



OPEN

# Atomic-Scale Fingerprint of Mn Dopant at the Surface of $\text{Sr}_3(\text{Ru}_{1-x}\text{Mn}_x)_2\text{O}_7$

SUBJECT AREAS:

CONDENSED-MATTER  
PHYSICSMATERIALS SCIENCE  
PHYSICSReceived  
20 May 2013Accepted  
13 September 2013Published  
10 October 2013Correspondence and  
requests for materials  
should be addressed to  
E.W.P. (wplummer@  
phys.lsu.edu)Guorong Li<sup>1</sup>, Qing Li<sup>2,3</sup>, Minghu Pan<sup>2</sup>, Biao Hu<sup>1</sup>, Chen Chen<sup>1</sup>, Jing Teng<sup>1</sup>, Zhenyu Diao<sup>1</sup>, Jiandi Zhang<sup>1</sup>, Rongying Jin<sup>1</sup> & E. W. Plummer<sup>1</sup><sup>1</sup>Department of Physics & Astronomy, Louisiana State University, Baton Rouge, Louisiana 70803, USA, <sup>2</sup>Center for Nanophase Materials Sciences, Oak Ridge National Laboratory, Oak Ridge, Tennessee 37831, USA, <sup>3</sup>Institute of Functional Nano & Soft Materials (FUNSOM), Soochow University, Suzhou, Jiangsu 215123, China.

Chemical doping in materials is known to give rise to emergent phenomena. These phenomena are extremely difficult to predict *a priori*, because electron-electron interactions are entangled with local environment of assembled atoms. Scanning tunneling microscopy and low energy electron diffraction are combined to investigate how the local electronic structure is correlated with lattice distortion on the surface of  $\text{Sr}_3(\text{Ru}_{1-x}\text{Mn}_x)_2\text{O}_7$ , which has double-layer building blocks formed by  $(\text{Ru}/\text{Mn})\text{O}_6$  octahedra with rotational distortion. The presence of doping-dependent tilt distortion of  $(\text{Ru}/\text{Mn})\text{O}_6$  octahedra at the surface results in a  $C_{2v}$  broken symmetry in contrast with the bulk  $C_{4v}$  counterpart. It also enables us to observe two Mn sites associated with the octahedral rotation in the bulk through the “chirality” of local electronic density of states surrounding Mn, which is randomly distributed. These results serve as fingerprint of chemical doping on the atomic scale.

Ruddlesden-Popper (RP) ruthenates  $\text{Sr}_{n+1}\text{Ru}_n\text{O}_{3n+1}$  ( $n = 1$  to  $\infty$ ) have attracted much attention because the strong coupling between charge, lattice, orbital, and spin degrees of freedom produces many exotic phenomena<sup>1,2</sup>. Similar to many other transition-metal compounds, partial chemical doping on either the Sr or Ru site can generate dramatic response in physical properties<sup>3–8</sup>. For example, as presented in Fig. 1 (a), partial replacement of Ru by Mn results in a metal-insulator transition (MIT) at  $T_{\text{MIT}}$  from metallic character at high temperatures to insulating behavior at low temperatures<sup>3,5</sup>. X-ray absorption spectroscopy reveals that the MIT drives the onset of local anti-ferromagnetic (AFM) correlations around the Mn sites<sup>9</sup>. The system eventually undergoes a magnetic phase transition from paramagnetic at high temperatures to long-range AFM ordering at  $T_{\text{M}}$ <sup>3,10</sup>. While these two transitions diverge with increasing Mn doping, the rotation angle  $\phi$  of  $(\text{Ru}/\text{Mn})\text{O}_6$  octahedra decreases from  $8^\circ$  in the parent compound ( $x = 0$ ) to  $0$  at  $x \sim 0.2$  (see Fig. 1a)<sup>3</sup>. This observation demonstrates that the electronic and magnetic properties are intimately coupled to the lattice structure (e.g. the rotation of octahedra).

The challenge is to understand how complex phenomena emerge from chemical doping. For RP ruthenates, first-principles calculations suggest that the electronic structure near the Fermi energy is determined by the structure of  $\text{RuO}_6$  octahedron<sup>11,12</sup>. Any change of the latter would impact the physical properties of the system<sup>11,12</sup>. For example, the rotation of  $\text{RuO}_6$  octahedron favors ferromagnetic (FM) metallic behavior, while the tilt distortion tends to drive the system into an AFM insulating state<sup>12</sup>. Such distortion of  $\text{RuO}_6$  octahedron can be tuned by non-thermal parameters such as chemical doping, pressure, and strain. Evidence for such structure-property correlation at the macroscopic scale has been observed in  $\text{Ca}_{2-x}\text{Sr}_x\text{RuO}_4$ <sup>4,13</sup>,  $(\text{Ca}_{1-x}\text{Sr}_x)_3\text{Ru}_2\text{O}_7$ <sup>8</sup> and  $\text{Sr}_3(\text{Ru}_{1-x}\text{Mn}_x)_2\text{O}_7$ <sup>3</sup>. However, microscopically, how the local density of states (LDOS) in general responds to the presence of dopants remains unanswered.

In this *Scientific Report*, we present the experimental investigation of chemical doping effect on both structure and LDOS at the surface of single crystal  $\text{Sr}_3(\text{Ru}_{1-x}\text{Mn}_x)_2\text{O}_7$ , with  $x = 0, 0.06$  and  $0.16$ . While low energy electron diffraction (LEED) is used to determine the lattice structure, scanning tunneling microscopy (STM) allows us to identify Mn sites and their impact on LDOS. We find that, in addition to the rotational distortion of octahedra seen in the bulk, there is tilt distortion at the surface. Thus the symmetry is reduced from  $C_{4v}$  in the bulk to  $C_{2v}$  at the surface which is observed in both LEED and STM. With STM, we observe the “chirality” in the LDOS at Mn sites resulting from rotation, but becoming visible because of the effects of tilt. The disturbance to LDOS (e.g. local electronic inhomogeneity) due to Mn depends dramatically on the doping concentration.

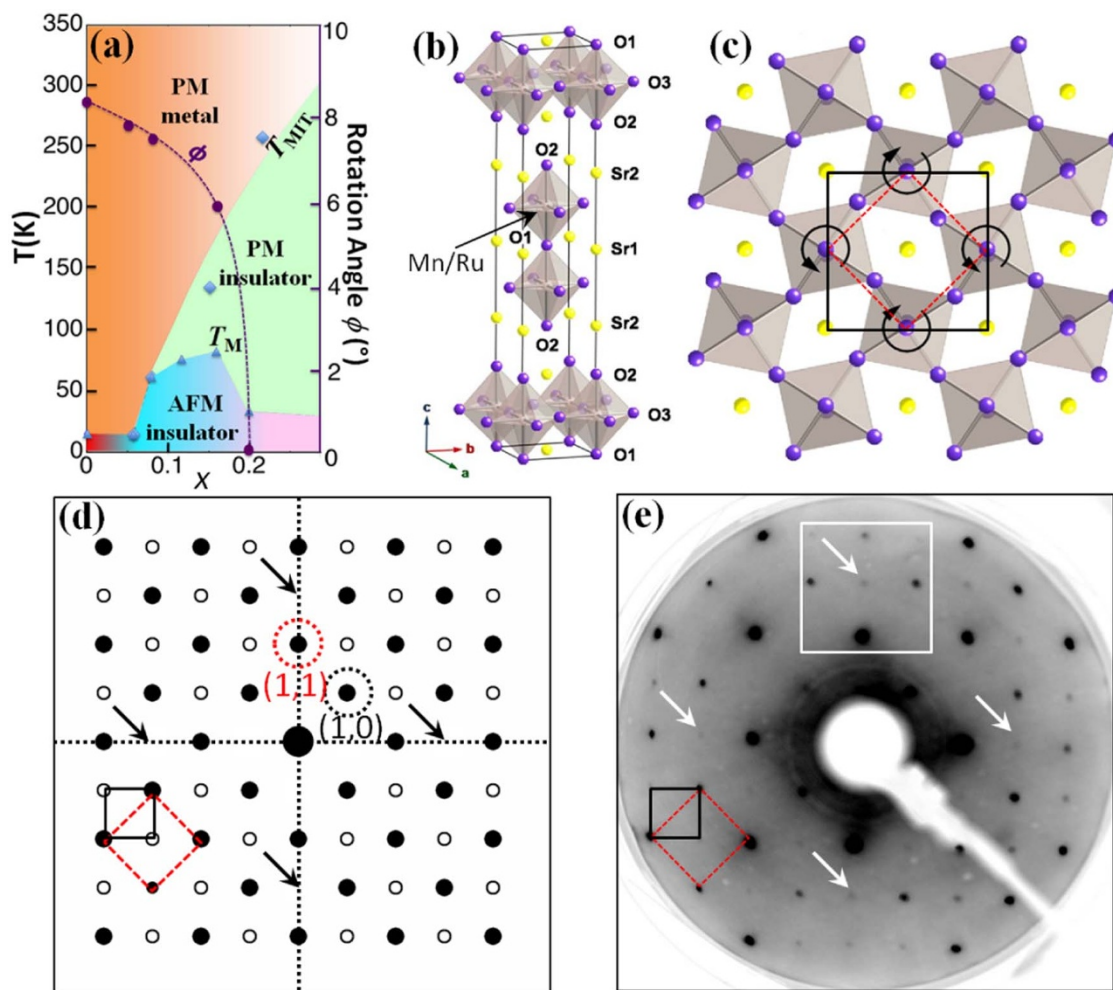


**Figure 1** | (a) Bulk phase diagram and (b) tetragonal (tet) unit-cell structure of  $\text{Sr}_3(\text{Ru}_{1-x}\text{Mn}_x)_2\text{O}_7$ . The Ru/Mn atoms are located in the center of each octahedron. (c) Top view of the surface plane and the first sub-surface ( $\text{Ru}/\text{Mn}$ ) $\text{O}_6$  octahedra layer. The octahedral rotations are indicated by arrows. The black square shows surface  $(\sqrt{2} \times \sqrt{2})\text{R}45^\circ$  unit cell, while red dashed square is the tet -  $(1 \times 1)$  unit cell. (d) A schematic LEED pattern expected for a surface with octahedral rotation but no tilt. The tet -  $(1 \times 1)$  real space periodicity generates diffractive spots (solid dots), where the  $(1, 1)$  and  $(0, 1)$  spots are labeled. The tet reciprocal unit cell is marked by the red dashed square. The  $(\sqrt{2} \times \sqrt{2})\text{R}45^\circ$  real space periodicity produces additional fractional spots (open circles), with a reciprocal lattice marked by a black square. The black dashed straight lines indicate the two glide lines, at which fractional spots are extinct as indicated by arrows. (e) An experimental image of LEED pattern taken at 87 K at 225 eV for  $\text{Sr}_3\text{Ru}_2\text{O}_7$  ( $x = 0$ ).

## Results

Due to their layered structure,  $\text{Sr}_3(\text{Ru}_{1-x}\text{Mn}_x)_2\text{O}_7$  single crystals cleave at the weak bonding between the double layers of octahedra (see Fig. 1b), exposing a Sr-O layer. Fig. 1c shows the top view of Sr-O terminated surface with the first sub-surface layer of octahedra, which are rotated by  $\sim 8^\circ$  in the bulk<sup>3,8</sup>. The rotation of octahedra at the surface is enhanced ( $\sim 12^\circ$ )<sup>14</sup>. The solid black line shows the primitive unit cell for bulk-truncation ( $5.6 \text{ \AA} \times 5.6 \text{ \AA}$ ). There are two Sr atoms in the unit cell (four corners), and two octahedral sites with one having clock-wise (*cw*) and the other counter-clock-wise (*ccw*) rotation, as indicated in Fig. 1c. The two Sr atoms in the unit cell are structurally identical, because there is no evidence for buckling of Sr atoms from LEED *I-V* analysis<sup>14,15</sup>. It is a standard procedure to use the notation associated with the tetragonal (tet) -  $(1 \times 1)$  unit cell (no rotation). This unit cell is shown by the red dashed square in Fig. 1c. In this nomenclature, which we will adapt for consistency, the primitive unit cell (black lines) is referred to as  $(\sqrt{2} \times \sqrt{2})\text{R}45^\circ$ .

If the surface has the same symmetry as the bulk (bulk-truncated), the LEED pattern should look like Fig. 1d<sup>14-16</sup>, where filled dots represent pattern expected from tet -  $(1 \times 1)$  structure, and open circles are fractional spots resulting from the  $(\sqrt{2} \times \sqrt{2})\text{R}45^\circ$  structure. Considering the structure factor, the fractional spots (circles)

are extinct along the two glide lines, represented by dashed lines in Fig. 1d. These glide lines were observed on the surface of  $\text{Sr}_2\text{RuO}_4$  due to  $9^\circ$  rotation of octahedron<sup>15</sup>. Under this rotational distortion, the surface still maintains  $C_{4v}$  symmetry. The LEED pattern for  $\text{Sr}_3\text{Ru}_2\text{O}_7$  ( $x = 0$ ) is shown in Fig. 1e. Note that there are no glide lines, expected for a bulk-truncated surface, indicating a change in the symmetry. According to our previous study<sup>14</sup>, the symmetry change is caused by tilt distortion of  $\text{RuO}_6$  octahedron by an angle  $\theta \approx 4.5^\circ$  at the surface (see Fig. 2a), reducing the surface symmetry to  $C_{2v}$ . There are two domains of tilt distortion which eliminates both glide lines.

As explained in our previous LEED *I-V* structure refinement for  $x = 0$ <sup>14</sup>, the relative intensity of the fractional spots with respect to the integral spots are proportional to the tilt angle. Therefore, the degree of tilt with Mn doping can be determined in the same manner, i.e., calculating the intensity of fractional spots appearing along the glide lines with respect to the integral spots. Figure 2b shows an enlarged image of LEED pattern marked by the white square in Fig. 1e for the parent compound ( $x = 0$ ). By normalizing the intensity of the fractional spot  $(3/2, 3/2)$  with respect to the integral spot  $(1, 2)$  [along the white dashed line of Fig. 2b], a line profile is obtained for  $x = 0$  and plotted in Fig. 2c (black). Applying the same procedure to doped

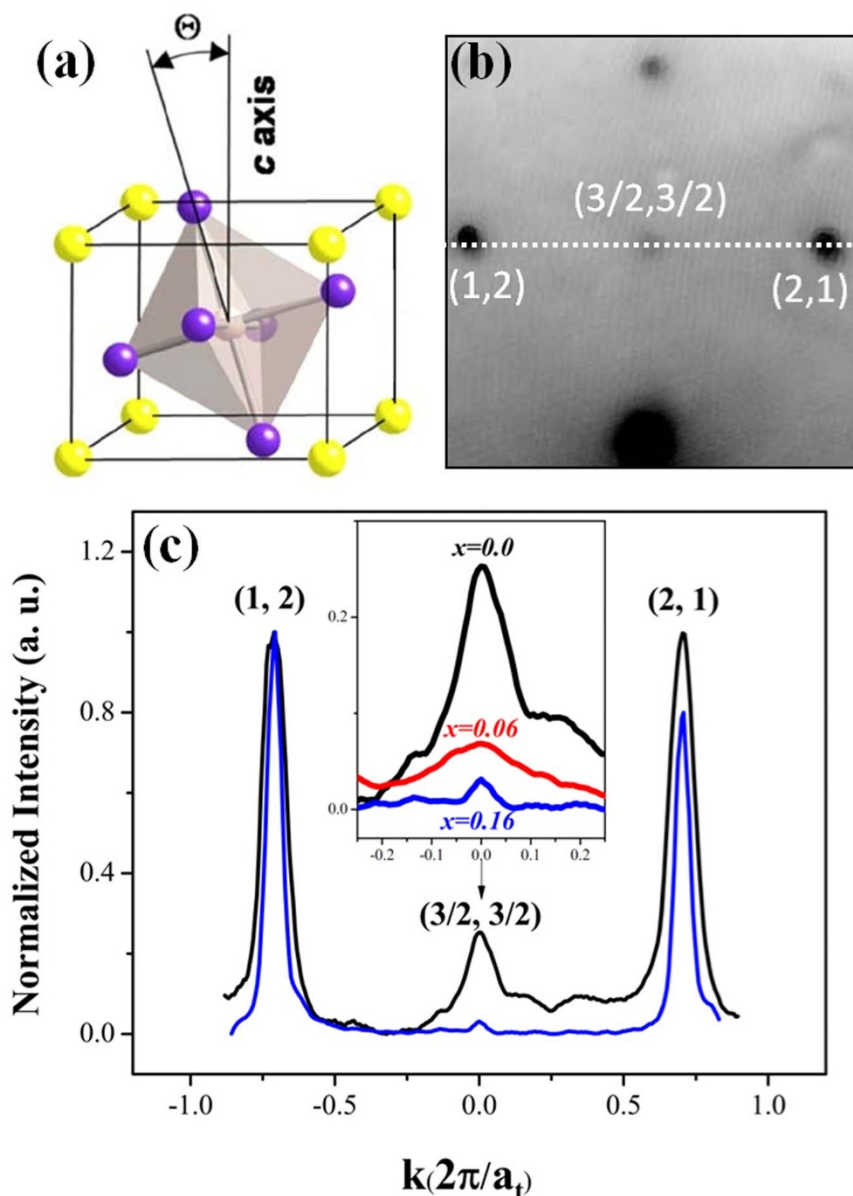


**Figure 2** | (a) Schematic view of tilt distortion in an octahedron with tilt angle ( $\theta$ ). (b) Enlargement of the white square marked in the LEED pattern in Fig. 1e, showing the integer spots (1, 2) and (2, 1) and the fractional order spot (3/2, 3/2) induced by tilt. (c) Normalized line profile along the dashed line in (b) for  $x = 0$  (black solid line) and 0.16 (blue solid line) at 87 K. The inset shows the doping dependence of the fractional spot intensity.

compounds, we find that the (3/2, 3/2) spot intensity decreases with increasing  $x$ . The inset of Fig. 2c displays the enlarged view of the relative intensity of the (3/2, 3/2) spot vs.  $x$ . This fractional spot intensity almost vanishes at  $x = 0.16$ , indicating a rapid reduction of tilt distortion with increasing doping level. By performing the same analysis for fractional spots associated with rotation distortion, we find no evidence for the doping dependence of the surface rotation down to  $\sim 80$  K. This implies the rotational distortion on the surface of  $\text{Sr}_3(\text{Ru}_{1-x}\text{Mn}_x)_2\text{O}_7$  ( $0 \leq x \leq 0.16$ ) remains unchanged. Note that the surface enhances the rotational angle  $\sim 12^\circ \pm 3^\circ$  for  $x = 0$ <sup>14</sup>, which is larger than its bulk counterpart ( $\sim 8^\circ$  at 90 K<sup>14</sup>). Consequently, a tilt distortion must occur in order to compensate the surface induced strain. This is consistent with neutron scattering measurements<sup>4,17</sup>, and first-principles calculations<sup>11,12,18</sup> on single-layered  $\text{Ca}_{2-x}\text{Sr}_x\text{RuO}_4$ , which indicates that tilt sets in after the rotation angle reaches  $12^\circ$ . Similar behavior has been reported for  $(\text{Sr}_{1-x}\text{Ca}_x)_3\text{Ru}_2\text{O}_7$  where a tilt distortion sets in at  $x = 0.4$ <sup>8</sup>. With this tilt distortion, the surface symmetry is reduced to  $C_{2v}$ .

The tilt of octahedra at the surface could have quite profound effects on the physical properties. First, tilt will always involve both of the bilayers in  $\text{Sr}_3(\text{Ru}_{1-x}\text{Mn}_x)_2\text{O}_7$  in contrast to rotation which could occur in one octahedral layer. Second, as explained in the introduction, tilt drives the system towards an insulating/AFM phase<sup>11,12</sup>. Finally, tilt distortion will break the symmetry shown in Fig. 1c, from  $C_{4v}$  to  $C_{2v}$ . Note that tilt does not change the size of the primitive unit cell, so there is surface reconstruction without a change in the unit cell. For comparison, we show the STM image of  $\text{Sr}_2\text{RuO}_4$  (Fig. 3a) where it is known that there is rotation but no tilt at the surface<sup>15</sup>. The bright protrusions in the images are associated with Sr atoms. The black square is the  $(\sqrt{2} \times \sqrt{2})R45^\circ$  unit cell shown in Fig. 1c. The image clearly shows  $C_{4v}$  symmetry as expected. The image of  $\text{Sr}_3\text{Ru}_2\text{O}_7$  shown in Fig. 3b is distinctly different from the image of  $\text{Sr}_2\text{RuO}_4$ : there are two kinds of hollow sites in  $\text{Sr}_3\text{Ru}_2\text{O}_7$  indicated by arrows, one slightly brighter than the other. This demonstrates that the symmetry of  $\text{Sr}_3\text{Ru}_2\text{O}_7$  (Fig. 3b) is  $C_{2v}$ , as expected from the surface structure with tilt. Similar features are seen

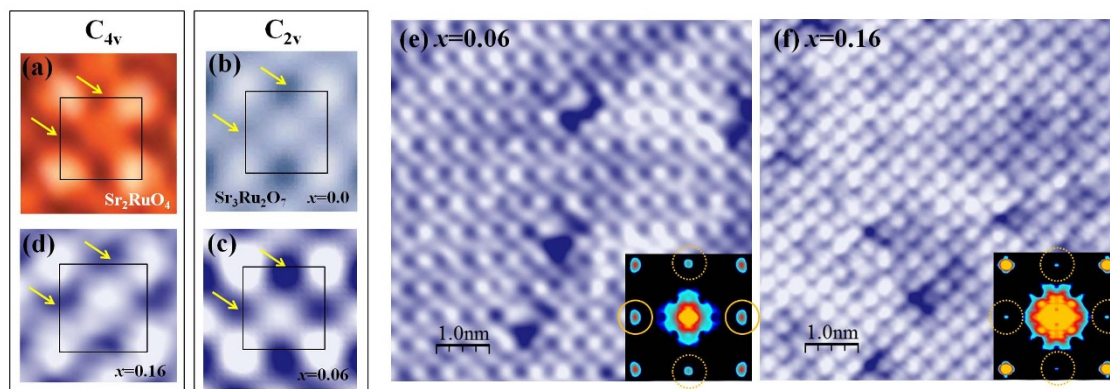


**Figure 3** | STM images with indicated symmetries for (a)  $\text{Sr}_2\text{RuO}_4$  at a bias of 0.75 V at 300 K, reproduced from Ref. 15, (b)  $\text{Sr}_3\text{Ru}_2\text{O}_7$  ( $x = 0$ ) at a bias of 7 mV at 0.56 K, reproduced from Ref. 7, (c)  $x = 0.06$ , for 0.9 V at 100 K, and (d)  $x = 0.16$ , at 0.6 V and 100 K. (e & f) 7.0 nm  $\times$  7.0 nm STM topography taken at 0.9 V (100 K) for  $x = 0.06$  and at 0.6 V (100 K) for  $x = 0.16$ . The insets are corresponding FFT images. The circled FFT spots are corresponding to fractional order spots from  $(\sqrt{2} \times \sqrt{2})\text{R}45^\circ$  structure. Note that the yellow dotted-line circled spots are less intense than solid-line circled ones for  $x = 0.06$ , indicating a broken symmetry.

in our study for  $x = 0.06$  as presented in Fig. 3c, even though the contrast difference of the two sites is reduced. As expected, the STM image for  $x = 0.16$  has  $C_{4v}$  symmetry as shown in Fig. 3d, because there is no longer tilt distortion at the surface. The different symmetry between  $x = 0.06$  and 0.16 is further illustrated in Figures 3e and 3f, both large-scale STM images with their fast Fourier Transform (FFT) images included in the insets. A casual inspection of STM and FFT images shows that  $x = 0.16$  has  $C_{4v}$  while  $x = 0.06$  has  $C_{2v}$  symmetry. The yellow dotted-line circled fractional spots are less intense compared to the solid-line circled spots in the FFT of  $x = 0.06$  in Fig. 3e. These spots are all the same for  $x = 0.16$  (Fig. 3f).

It should be mentioned that the low temperature and low bias STM images of  $x = 0$  (Fig. 3b)<sup>7</sup> and 0.06 (Fig. 3c) display different intensity for the two Sr atoms in the unit cell. While this could result from the presence of tilt, the unanswerable question is why high quality STM images of  $\text{Sr}_3\text{Ru}_2\text{O}_7$ <sup>6</sup> show that both Sr atoms in the unit cell have the same intensity. An even more perplexing observation is that STM images from  $\text{Sr}_3\text{Ru}_2\text{O}_7$  doped with 1% Ti<sup>6</sup> display perfect  $C_{4v}$  symmetry. It is unlikely that 1% Ti concentration in  $\text{Sr}_3\text{Ru}_2\text{O}_7$  removes the tilt of octahedra at the surface. Obviously, a detailed surface structural analysis and more fundamental understanding of STM imaging have to be undertaken.

The presence of subsurface Mn substituted for Ru creates the dark defect regions shown in Fig. 3e for  $x = 0.06$  and Fig. 3f for  $x = 0.16$  sample. The spatial resolution of the details in STM images of the electronic disturbance caused by Mn is very sensitive to the bias voltage. Fig. 4a shows an image for  $x = 0.06$  sample with bias of 1.2 V. At this bias, Mn impurities appear as bright spots surrounded by dark regions of different chirality. Fig. 4b shows an enlarged image of the region marked in Fig. 4a. The lattice  $[(\sqrt{2} \times \sqrt{2})\text{R}45^\circ]$  is drawn with the grid of black lines, but shifted by half unit cell compared to Fig. 1c. The two Mn sites with different chirality are now positioned at the center and corner of the grid, respectively. The different chirality in the LDOS in the region surrounding the Mn atom is clear and illustrated in Fig. 4b. The Mn site at the corner shows *ccw* chirality while the Mn atom at the center of the grid has *cw* chirality. In stark contrast, the images for  $x = 0.16$  sample do not exhibit an extended spatial electronic disturbance associated with each Mn (Fig. 4c). In fact for several lower bias voltages one only sees the Sr ordered lattice (for example, Fig. 3f). Fig. 4c shows an image at 1.0 V bias for  $x = 0.16$  sample where the Mn atoms appear as bright dots. Fig. 4d presents an image of the square marked in Fig. 4c with the lattice included. Using the chirality notation from Fig. 4b, each site can be labeled by lines (*ccw*) and circles (*cw*), respectively. Even though it is not possible to see the chirality, we can determine the sites from

the position of the Mn atom with respect to the lattice. The chirality (site) of each Mn atom is identified in Fig. 4c and Fig. 4d.

These features in the STM images scale with the Mn doping level and statistical analysis shows that Mn is randomly distributed at the surface without any sign of clustering. We count and histogram all Mn sites as a function of Mn-Mn distance, normalized by the histogram of a random model with the same number of doping sites<sup>19</sup> (the random model was simulated 1000 times to reduce the error). This results in so-called radial distribution ratio (RDR). RDR = 1 indicates there is no clustering. Fig. 4e shows RDR curves for  $x = 0.06$  and  $x = 0.16$ , respectively. As both show RDR close to 1, we conclude there is no clustering of Mn at both doping levels. The statistical analysis also shows that the distribution of the two different sites is random and equal.

## Discussion

There is an issue associated with the observed concentration of chemical doping. Our counting gives a value of  $(2.6 \pm 0.6)\%$  for  $x = 0.06$  sample and  $(11.4 \pm 2.2)\%$  for the  $x = 0.16$  sample, where the error bars come from the statistics variance on the average number ( $n$ ) of doping sites is  $(\sqrt{n})$  assuming that they are randomly distributed with confidence level of 95%. Our analysis on the published data<sup>6</sup> for the 1% Ti doped sample shows  $\sim 0.5\%$  Ti in the top layer and  $\sim 0.8\%$  in the second layer. There are at least two possibilities: (1) cleaving creates a surface with a different concentration than in the bulk, or (2) doping is not uniform in the bulk.

Two main issues remain: Why are the STM images of  $x = 0.06$  and 0.16 so different, and what is the role of the broken symmetry created by the tilt in electronic chirality of Mn sites for  $x = 0.06$ ? Based on our STM images, the size of inhomogeneity in the LDOS is larger than 2 unit cells for  $x = 0.06$  (Fig. 4b) and less than one unit cell for  $x = 0.16$  (Fig. 4d). This indicates that the electronic inhomogeneity is more localized for  $x = 0.16$ . Theoretically this is what is expected when tilt is present<sup>18</sup>. The presence of tilt favors an AFM insulating phases<sup>18</sup>, thus lowering the electrical conductivity. The reduced electrical conductivity enhances screening length, allowing us to easily image the effect of Mn sites. Recently, electronic chirality has also been reported for  $\text{Sr}_3\text{Ir}_2\text{O}_7$ , due to missing apical oxygen in  $\text{IrO}_6$  octahedra<sup>20</sup> for a surface that appears to be semiconducting. The question related to this study is whether the nature of the semiconducting surface is associated to possible surface structural distortion.

In summary, the combined LEED and STM approach allows us to investigate the correlation between crystallographic and electronic structure on the atomic scale at the surface of  $\text{Sr}_3(\text{Ru}_{1-x}\text{Mn}_x)_2\text{O}_7$ . While the bulk has  $C_{4v}$  symmetry, the surface of  $\text{Sr}_3(\text{Ru}_{1-x}\text{Mn}_x)_2\text{O}_7$  exhibits broken  $C_{2v}$  symmetry due to a tilt distortion of  $(\text{Ru}/\text{Mn})\text{O}_6$

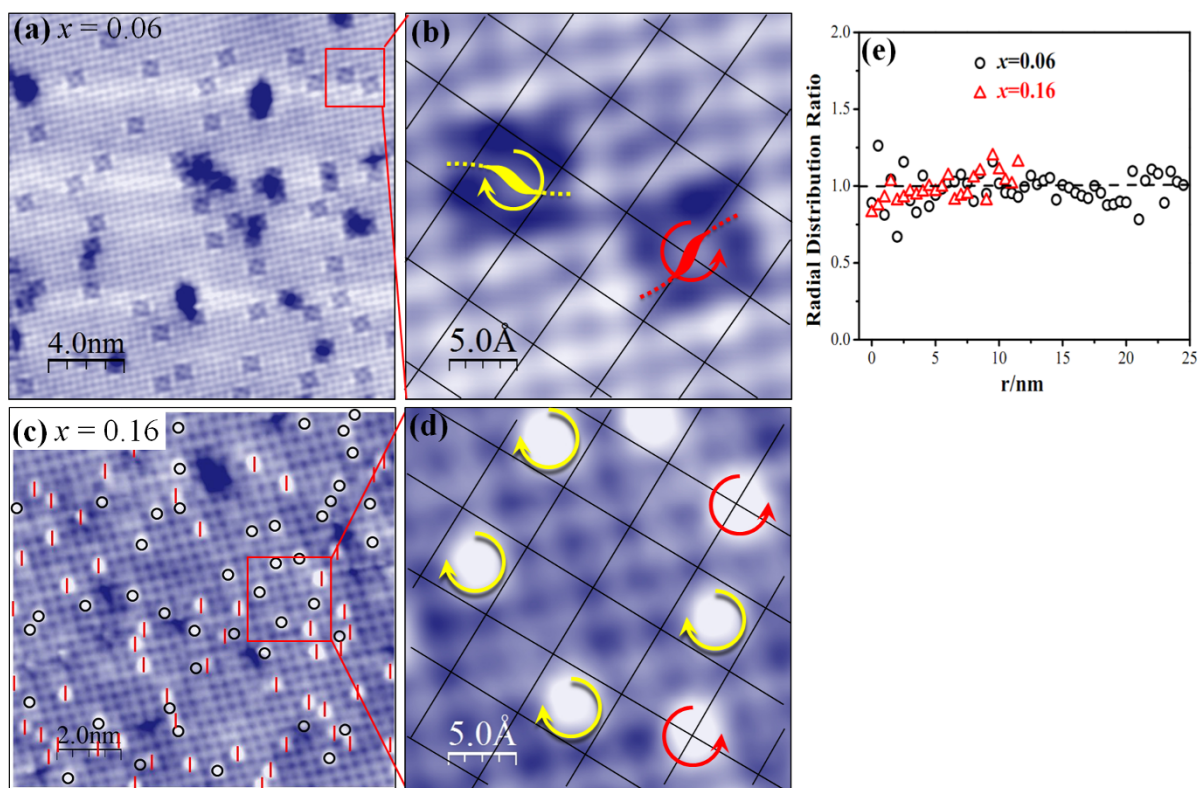


**Figure 4** | (a) STM topography of  $x = 0.06$  compound taken at +1.2 V (100 K). (b) The zoom-in STM topographic image from the marked square region in (a) with the orthorhombic lattice grid (black solid lines). The different chirality of the Mn sites is indicated. (c) STM topography of  $x = 0.16$  compound taken at 1.0 V (100 K). (d) The zoom-in STM topographic image from the red square region in (c) with the lattice grid. The chirality is shown by arrows, using the notation of (b). (e) Radial distribution ratio for  $x = 0.06$  (circles), and 0.16 (triangles).

octahedra for  $x < 0.16$ . While the rotation angle remains unchanged at the surface, the tilt angle decreases with increasing Mn doping concentration, nearly vanishing at  $x = 0.16$ . The effect of tilt is observed in the STM images and the corresponding FFT showing the  $C_{2v}$  symmetry. Although Mn is homogeneously distributed, our STM results reveal a local electronic inhomogeneity that has the chirality caused by the rotations of octahedra, but becoming visible because of the effects of tilt. The physics is simple and beautiful. On the surface of parent compound, there is a tilt distortion, which favors an insulating phase. The introduction of Mn-doping gradually diminishes the surface-induced tilt and thus increases surface metallicity. As the metallicity increases, the effect of electronic inhomogeneity induced by Mn diminishes. This explains why the LDOS effects due to the sub-surface Mn sites are more observable at the surface of  $x = 0.06$  than  $x = 0.16$ . The fingerprints of Mn dopant we observed will advance the fundamental understanding at the atomic level of the complexity induced by doping.

## Methods

$\text{Sr}_3(\text{Ru}_{1-x}\text{Mn}_x)_2\text{O}_7$  ( $x = 0, 0.06, 0.16$ ) single crystals are grown using the floating-zone technique in an image furnace, with details described elsewhere<sup>2</sup>. For each doping level, we use samples from the same growth batch for STM, LEED, and transport experiments. All LEED and STM experiments are conducted in an ultra-high vacuum with base pressure  $< 2 \times 10^{-10}$  Torr but in different chambers. For LEED experiments, samples are mounted on a variable temperature manipulator and are cleaved at 87 K. The LEED pattern and intensity ( $I$ ) - voltage ( $V$ ) curves are collected at 87 K with Omicron LEED optics and a CCD camera. STM measurements are carried out in a home-built and variable temperature system with a Pt-Ir tip<sup>21,22</sup>. Single crystal samples are first pre-cooled to 100 K, cleaved, and then immediately inserted into the pre-cooled STM stage.

1. Dagotto, E. Complexity in strongly correlated electronic systems. *Science* **309**, 257 (2005).

- Cao, G., Alexander, C. S., McCall, S., Crow, J. E. & Guertin, R. P. From antiferromagnetic insulator to ferromagnetic metal: a brief review of the layered ruthenates. *Mater. Sci. Eng. B* **63**, 76 (1999).
- Hu, B. *et al.* Structure-property coupling in  $\text{Sr}_3(\text{Ru}_{1-x}\text{Mn}_x)_2\text{O}_7$ . *Phys. Rev. B* **84**, 174411 (2011).
- Friedt, O. *et al.* Structural and magnetic aspects of the metal-insulator transition in  $\text{Ca}_{2-x}\text{Sr}_x\text{RuO}_4$ . *Phys. Rev. B* **63**, 174432 (2001).
- Mathieu, R. *et al.* Impurity-induced transition to a Mott insulator in  $\text{Sr}_3\text{Ru}_2\text{O}_7$ . *Phys. Rev. B* **72**, 092404 (2005).
- Lee, J. *et al.* Heavy d-electron quasiparticle interference and real-space electronic structure of  $\text{Sr}_3\text{Ru}_2\text{O}_7$ . *Nature Phys.* **5**, 800 (2009).
- Iwaya, K. *et al.* Local tunneling spectroscopy across a metamagnetic critical point in the bilayer ruthenate  $\text{Sr}_3\text{Ru}_2\text{O}_7$ . *Phys. Rev. Lett.* **99**, 057208 (2007).
- Peng, J. *et al.* Interplay between the lattice and spin degrees of freedom in  $(\text{Sr}_{1-x}\text{Ca}_x)_3\text{Ru}_2\text{O}_7$ . *Phys. Rev. B* **82**, 024417 (2010).
- Hossain, M. A. *et al.* Crystal-field level inversion in lightly Mn-doped  $\text{Sr}_3\text{Ru}_2\text{O}_7$ . *Phys. Rev. Lett.* **101**, 016404 (2008).
- Mesa, D. *et al.* Single-bilayer E-type antiferromagnetism in Mn-substituted  $\text{Sr}_3\text{Ru}_2\text{O}_7$ : neutron scattering study. *Phys. Rev. B* **85**, 180410 (2012).
- Fang, Z., Nagaosa, N. & Terakura, K. Orbital-dependent phase control in  $\text{Ca}_{2-x}\text{Sr}_x\text{RuO}_4$  ( $0 < x < \sim 0.5$ ). *Phys. Rev. B* **69**, 045116 (2004).
- Fang, Z. & Terakura, K. Magnetic phase diagram of  $\text{Ca}_{2-x}\text{Sr}_x\text{RuO}_4$  governed by structural distortions. *Phys. Rev. B* **64**, 020509 (2001).
- Nakatsuji, S. & Maeno, Y. Quasi-two-dimensional Mott transition system  $\text{Ca}_{2-x}\text{Sr}_x\text{RuO}_4$ . *Phys. Rev. Lett.* **84**, 2666–2669 (2000).
- Hu, B. *et al.* Surface and bulk structural properties of single-crystalline  $\text{Sr}_3\text{Ru}_2\text{O}_7$ . *Phys. Rev. B* **81**, 184104 (2010).
- Matzdorf, R. *et al.* Ferromagnetism stabilized by lattice distortion at the surface of the p-wave superconductor  $\text{Sr}_2\text{RuO}_4$ . *Science* **289**, 746 (2000).
- Moore, R. G. *et al.* A Surface-Tailored, Purely Electronic, Mott Metal-to-Insulator Transition. *Science* **318**, 615 (2007).
- Braden, M., André, G., Nakatsuji, S. & Maeno, Y. Crystal and magnetic structure of  $\text{Ca}_2\text{RuO}_4$ : Magnetoelastic coupling and the metal-insulator transition. *Phys. Rev. B* **58**, 847 (1998).
- Fang, Z., Terakura, K. & Nagaosa, N. Orbital physics in ruthenates: first-principles studies. *New J. Phys.* **7**, 66 (2005).
- Zeljovic, I. *et al.* Nanoscale surface element identification and dopant homogeneity in the high- $T_c$  superconductor  $\text{Pr}_x\text{Ca}_{1-x}\text{Fe}_2\text{As}_2$ . *Phys. Rev. B* **87**, 201108(R) (2013).



20. Okada, Y. *et al.* Imaging the evolution of metallic states in a spin-orbit interaction driven correlated iridate. *Nature Mat.* **12**, 707 (2013).
21. Stipe, B. C., Rezaei, M. A. & Ho, W. A variable-temperature scanning tunneling microscope capable of single-molecule vibrational spectroscopy. *Rev. Sci. Instrum.* **70**, 137 (1999).
22. Pan, S. H., Hudson, E. W. & Davis, J. C. <sup>3</sup>He refrigerator based very low temperature scanning tunneling microscope. *Rev. Sci. Instrum.* **70**, 1459 (1999).

## Acknowledgements

Research at LSU is supported by NSF DMR-1002622 (GL, RJ, EWP) and NSF DMR-1005562 (JZ). Part of this research was conducted (QL, MP) at the Center for Nanophase Materials Sciences, which is sponsored at Oak Ridge National Laboratory by the Scientific User Facilities Division, Office of Basic Energy Sciences, U.S. Department of Energy. We would like to thank R. Kurtz for constructive discussions.

## Author contributions

G.L., Q.L., M.P., C.C. and J.T. took and analyzed the data. B.H. and Z.D. synthesized the crystals, G.L., J.Z., R.J. and E.W.P. wrote the manuscript.

## Additional information

**Competing financial interests:** The authors declare no competing financial interests.

**How to cite this article:** Li, G. *et al.* Atomic-Scale Fingerprint of Mn Dopant at the Surface of Sr<sub>3</sub>(Ru<sub>1-x</sub>Mn<sub>x</sub>)<sub>2</sub>O<sub>7</sub>. *Sci. Rep.* **3**, 2882; DOI:10.1038/srep02882 (2013).



This work is licensed under a Creative Commons Attribution-NonCommercial-NoDerivs 3.0 Unported license. To view a copy of this license, visit <http://creativecommons.org/licenses/by-nc-nd/3.0>